Annals of 3D Printed Medicine 18 (2025) 100196

Contents lists available at ScienceDirect

Annals of 3D Printed Medicine

journal homepage: www.elsevier.com/locate/stlm

Research paper

Development of 3D-printed flow-diverting stents for studying the effect of aneurysm treatment *in vitro*

Lana Bautz [a], Oluwabusayo A. Oni [b], Tamim Sarwar [a], Hivnu Toraman [c], Olav Jansen [c], Jan-Bernd Hövener [a], Naomi Larsen [c], Mariya S. Pravdivtseva [a,*]

[a] Department of Radiology and Neuroradiology, Section Biomedical Imaging, Molecular Imaging North Competence Center (MOIN CC), University Medical Center Schleswig-Holstein, Kiel University, Kiel, Germany
[b] The Carle Illinois College of Medicine, University of Illinois Urbana-Champaign, Champaign, IL, United States of America, USA
[c] Department of Radiology and Neuroradiology, University Medical Center Schleswig-Holstein, Kiel, Germany

ARTICLE INFO

Keywords:
Intracranial aneurysm
Endovascular treatment
Flow-diverting stents
3D printing
Magnetic resonance imaging

ABSTRACT

Background: Intracranial aneurysms (IAs) are preventively treated with flow-diverting stents (FDs), but complications persist, necessitating safer, customized FDs. While 4D flow magnetic resonance imaging (MRI) can evaluate FD treatment efficiency, metal artifacts from FDs compromise flow assessments.
Purpose: This study developed a protocol for fabricating 3D-printed FD replicas to test customized FDs and support MR imaging development by providing a metal-free testing platform.
Methods: Simplified mesh models with varying wire diameters (0.05–0.5 mm) and cell lengths (0.07–4.74 mm) were 3D printed using stereolithography and tested under gravity. A patient-specific aneurysm model was created, with 3D-printed FDs featuring 6, 16, and 20 wires covering the aneurysm entrance. Flow reduction caused by 3D printed FDs was evaluated with 4D flow MRI and compared to a commercial FD.
Results: Printable meshes had wire diameters $\geq$ 0.05 mm, with porosities over 14 % ensuring permeability. Lower porosities reduced gravity flow (4.93 ml/s vs. 28.57 ml/s for 14 % and 54 % porosity). Only wire sizes of 0.25 mm and 0.5 mm were accurately 3D-printed. The 3D-printed FDs reduced flow into the aneurysm sac without metal artifacts on MR images. The 20-wire FD fully occluded aneurysm flow, while the 16-wire and 6-wire FDs achieved 94 % and 76 % reductions, comparable to the 65 % reduction of the commercial FD.
Conclusion: The proposed workflow enables efficient 3D printing of FD replicas that match commercial FDs in performance. These 3D-printed FDs can optimize initial design parameters and support artifact-free MR imaging development for aneurysm treatment evaluation.

1. Introduction

Intracranial aneurysms (IAs) are dilations of brain arterial vessels and present a prevalence of about 3 % in the adult population [1,2]. If an IA ruptures, an aneurysmal subarachnoid hemorrhage develops, which is associated with a 30-day death rate of 45 % [3]. Therefore, effective and safe treatment of unruptured IAs is required to occlude them while maintaining blood flow in the adjacent vessels. IAs are treated surgically, for example, by clipping with optional bypass techniques or by applying endovascular methods and placing devices that modulate flow. Endovascular methods include coiling, intrasaccular flow disruption, and intravascular flow diversion [4].

Flow-diverting stents (FDs) are braided mesh stents designed to divert flow from the aneurysm sac and reconstruct the parental vessel segmentally at the level of the aneurysm neck. Due to the reduction in aneurysmal flow, intra-aneurysmal thrombosis subsequently occurs [4–6]. In recent years, FDs have proven to be reliable in treating IAs, with aneurysm occlusion rates of over 80 % at follow-up. However, morbidity and mortality rates of 8.6 % and 3.1 %, respectively, have been reported [7–12]. Furthermore, periprocedural adverse events with a total complication rate of up to 22 % have also been documented [13], including delayed aneurysm rupture, in-stent stenosis, and subsequent

Footnote: Present affiliation: Lana Bautz, Klinikum Dortmund, Dortmund, Germany; Tamim Sarwar, Faculty of Engineering, Kiel University, Kiel, Germany
* Corresponding author at: Arnold-Heller-Straße 3, Haus 41, D-24105 Kiel, Germany.
E-mail addresses: lana.bautz@uni-wh.de (L. Bautz), oni2@illinois.edu (O.A. Oni), tasa@tf.uni-kiel.de (T. Sarwar), olav.jansen@uksh.de (O. Jansen), jan.hoevener@rad.uni-kiel.de (J.-B. Hövener), naomi.larsen@uksh.de (N. Larsen), mariya.pravdivtseva@rad.uni-kiel.de (M.S. Pravdivtseva).

https://doi.org/10.1016/j.stlm.2025.100196
Received 23 November 2024; Accepted 19 February 2025
Available online 5 March 2025
2666-9641/© 2025 The Authors. Published by Elsevier Masson SAS. This is an open access article under the CC BY-NC-ND license (http://creativecommons.org/licenses/by-nc-nd/4.0/).

stroke [10–12].

Current FDs are generic, and there are limited options for customization, e.g., adjusting length or diameter, to meet individual patient needs. Thus, therapy may fail due to insufficient aneurysmal flow reduction. Moreover, IAs vary substantially in shape and size, rendering generic FDs less effective for treating individual patients.

Therefore, new and safer FDs are constantly being developed. Nevertheless, the fabrication and testing of each FD prototype is labor-intensive, time-consuming, costly, and requires extensive animal testing. To streamline the development of FDs, they can be tested using structural numerical analysis and computational fluid dynamics (CFD) simulations [14]. Zhang et al. proposed an optimization strategy for FDs, maximizing blockage of aneurysmal inflow while maintaining porosity tailored to each patient [15]. Fu et al. studied virtual stents with regard to different structures and wire cross-sections [16], while Janiga et al. introduced a FD optimization principle to assist physicians in devising patient-specific treatments [17]. However, accurate deployment of a virtual implant requires a detailed 3D description of the "device/vessel wall/flowing blood" interaction, which is not yet available [18]. Nevertheless, virtual deployment and flow analysis by simulation is a rapid process that can produce clinically relevant results [19]. Still, the optimized results of virtual tests cannot always be reproduced *in vivo*.

Therefore, as a next step, FD prototypes selected based on simulation results need to be evaluated *in vitro* within aneurysm models before *in vivo* testing. *In vitro* testing of FD prototypes can create a more realistic device deployment scenario and evaluate flow reduction with methods such as 4D flow magnetic resonance imaging (MRI) that can be applied *in vivo* [20]. Therefore, the likelihood of being able to transfer results from *in vitro* to *in vivo* is higher. However, to perform *in vitro* tests, FD prototypes must first be produced. Conventional methods such as braiding or thin-film technology are time-consuming and costly when design changes are implemented.

Thus, we propose using 3D printing to produce FD prototypes. We hypothesize that optimizing parameters using 3D-printed prototypes and vessel replicas should precede the fabrication of real devices for *in vitro* and *in vivo* testing. This approach would potentially reduce the number of design iterations with real devices and *in vivo* experiments. Additionally, 3D-printed implants could be used to test and validate *in vivo* imaging methods like MRI, which are sensitive to metal artifacts from implants [21,22]. They could also serve as a platform for verifying results from virtual deployment and flow analysis conducted using CFD [23,24].

This work aims to develop a protocol for fabricating 3D-printed FD replicas tailored to patient-specific aneurysm models. These 3D-printed FDs can be used to optimize stent design parameters, test customized devices, and contribute to developing MR imaging techniques for aneurysm treatment evaluation by providing a metal-free testing platform.

2. Materials and methods

2.1. FD mimicking 3D-printed mesh structures

A simplified model mimicking commercial FDs was designed as a 3D mesh-like structure consisting of two parallel arrays of circular wires arranged perpendicular to each other (Fig. 1A, Autodesk Inventor Professional 2023, Autodesk Inc., San Rafael, California, USA). The wire diameters and side lengths of the square mesh cells were chosen to achieve mesh porosities between 10 and 80 %, considering the limitations of the 3D printer available. The dimensions of the computer-aided design (CAD) values of the wire diameters and side lengths of mesh cells ranged from 0.05 to 0.5 mm and 0.07 to 4.74 mm, respectively (Table 1). The minimum wire diameter (0.05 mm) was twice the spatial resolution of the stereolithographic (SLA) 3D printer used (0.025 mm, Form 3B, Formlabs, Somerville, Massachusetts, US). Note that the porosity range considered is consistent with the porosity values specified for commercially available FDs (30–70 %) [8,25].

Next, to test the general permeability of the designed meshes and their effect on the flow, meshes were embedded in 1) a bottle cap (Fig. 1B) and 2) a straight tube (Supplementary Material, Section S.1.1., Figure S.1A) and then 3D printed.

All models used in this study were 3D printed with a synthetic resin material with a layer thickness of 0.025 mm using the SLA 3D printer [75–90 % methacrylated oligomer, 25–50 % methacrylated monomer, and 1 % diphenyl (2,4,6-trimethylbenzoyl) phosphine oxide].

Table 1
Nominal digital dimensions of cell length and wire diameters of the CAD meshes.

Wire diameter [mm]	Square cell length [mm] for specific porosity					
	10 %	30 %	50 %	60 %	70 %	80 %
0.05	0.07	0.11	0.17	0.22	0.31	0.47
0.1	0.15	0.22	0.34	0.44	0.61	0.95
0.25	0.37	0.55	0.85	1.11	1.53	2.37
0.5	0.73	1.11	1.71	2.22	3.06	4.74

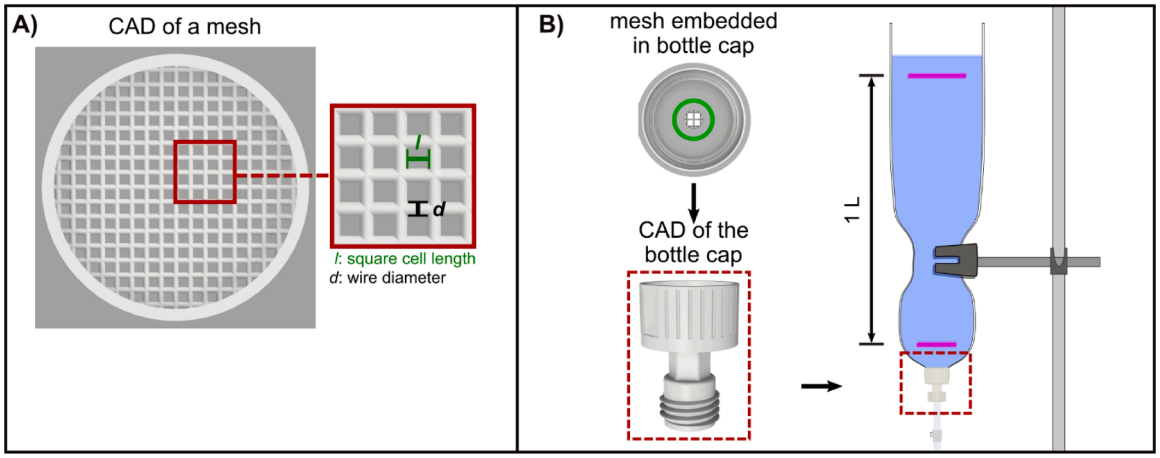

Fig. 1. Overview of the test models and setups used to determine the general permeability of the meshes and their influence on the flow rate. A) Exemplary computer-aided design (CAD) of a mesh with a wire diameter of 0.05 mm (d, black line) and a cell length of 0.73 mm (l, green line). B) Experimental setup for testing the permeability of the 3D-printed meshes as a function of wire diameter and porosity. Bottle caps with embedded meshes (green circle) were connected to a silicone tube with a quick-release closure and screwed onto a PET bottle (red rectangle). The bottle was stabilized upside down so that liquid could be dispensed under gravity conditions.

2.2. Determination of the porosity of 3D-printed meshes

To assess the physical porosity of the meshes after 3D printing, images of the meshes along with a ruler were acquired using a video microscope (magnification ratio 7.1:1, zoom 0.7x, OIV 254, Kern & Sohn GmbH, Balingen, Germany).

The resulting images were binarized using an adaptive threshold method [26,27] to separate printed structures and mesh holes. A threshold value of $n = 250$ contiguous pixels was chosen to automatically identify the holes, whereupon their area was determined individually (Supplementary Material, Section S.1.2, Figure S.2). The physical porosity was calculated as porosity $= \frac{\text{area}_{\text{open}}}{\text{area}_{\text{total}}} \cdot 100\ \%$, where $\text{area}_{\text{open}}$ represents the summed areas of the holes and $\text{area}_{\text{total}}$ the total area of the circular mesh with a diameter of 6 mm. To convert pixels to millimeters, the bar-to-bar distance on the ruler was measured five times by manually drawing a line and then averaging.

The wire diameter in the binary image was measured manually five times to obtain a mean value for the physical wire diameter. In addition, the height and width of five different cavities in the meshes were measured to determine the mean square cell length. Images were processed in MATLAB (R2022a, The Mathworks Inc., Natick, Massachusetts, USA).

2.3. Mesh permeability testing

The bottle caps were screwed onto a conventional 1.5 L polyethylene terephthalate (PET) bottle placed upside down in a stand and filled with a water/glycerol mixture [40/60 % volume, viscosity $\eta = 3.7$ cP [28] to mimic blood viscosity [29]. The liquid quantity of 1 L was marked by pink stripes on the bottle (Fig. 1B). The narrow outlet of the bottle cap was connected to a silicone tube, which was closed by a plug. When the plug was removed, the liquid flowed through the mesh due to gravity. If there was no liquid outflow, then the mesh was considered impermeable and excluded from further analysis.

The liquid outflow was recorded with a video camera [50 frames per second (fps), Sony Alpha 6400, Sony Group Corporation, Minato, Tokyo, Japan]. For each mesh, the permeability test was repeated six times. By manually tracking the liquid's outflow by video recording, the time required for the liquid to pass between the pink stripes was measured. This determined the time needed for 1 L of liquid to flow through the mesh. After that, the flow rate through the mesh was determined by dividing the liquid volume (1 L) by the resulting time.

In addition, the permeability of the meshes was tested under physiological flow-conditions [30] at mean flow rates of 2.5, 4.2, and 5.8 ml/s with a period of 1 s set by a pulsatile pump (PD-1100, BDC Laboratories, Wheat Ridge, Colorado, USA). Details of this experiment described in Supplementary Material, Section S.1.1.

2.4. Statistical analysis

The dependence of the flow rate through the mesh on its porosity in the general permeability test was fitted using a linear function. In addition, the Bravais-Pearson correlation coefficient and the associated significance value (p-value) were determined.

The median, first and third quartiles are reported to summarize the statistics and variability of all experimental data collected. MATLAB (R2022a, The Mathworks Inc., Natick, Massachusetts, USA) was used for the statistical analysis and to create the graphical representations.

2.5. Production of 3D-printed flow-diverting stents

FDs suitable for treating a specific aneurysm are selected according to the location and geometry of that aneurysm and its adjacent vasculature. Therefore, an exemplary patient-specific aneurysm was first selected to design a 3D-printed FD that fits this particular vascular geometry (Fusion360, Autodesk, Inc., Mill Valles, California, USA). Although the protocol is demonstrated and evaluated on one aneurysm geometry, none of the steps described depends on that, rendering the protocol applicable to any aneurysm geometry.

2.5.1. Design of patient-specific aneurysm model

The patient-specific aneurysm model of a paraophthalmic aneurysm of the left ICA (max. dimension 14 mm) was designed in-house [31,32]. Briefly described, the aneurysm sac and adjacent vessel lumen of this patient was segmented through a threshold-based region-growing algorithm [33] from the clinical 3D rotational angiography data of a patient (58 yr, female, x-ray angiographic system, Allura Xper FD20/10 biplane, Philips Healthcare, Best, Netherlands, Version R7.2.7). The resulting scalar mask was used to generate a digital vessel by using a marching cubes algorithm [34]. The resulting digital vasculature was simplified by cutting branches about 3 cm distally from the aneurysm neck.

2.5.2. Design of 3D-printed flow-diverting stents

FDs are braided, flexible, tubular structures implanted into the aneurysm's parental vessel to reconstruct the healthy course of the vessel. The digital design of the 3D-printed FDs follows the procedure described below (Fig. 2):

1. *Reconstruction of the healthy vessel.* The course of the healthy vessel was laid out at the location of the aneurysm as follows:
   a. Central points of the unaffected section of the healthy vessel were defined starting from the region before to after the aneurysm.
   b. By connecting the central points via a *spline,* a centerline was designed to reconstruct the vessel.
   c. Two cross-sectional profiles were placed perpendicular to the centerline, one at each end of the previously established boundaries of the vessel lumen.
   d. The missing vessel section was created by connecting the designed 2D profiles, following the centerline course (Fig. 2, step 1).
2. *Design of the braided stent structure.* The stent was digitally created by wrapping wires around the reconstructed vessel; this requires the following:
   a. Points indicating the beginning of the wires were placed equidistantly at the 2D profile in the region before the aneurysm (Fig. 2, step 2).
   b. Starting from each point, a helical wire was placed around the reconstructed vessel. Every second wire was twisted clockwise, the others counterclockwise (Fig. 2, step 3).
   c. The number of wires, wire thickness, and the angle of the helix are variable to achieve the desired porosity and flow reduction.
3. *Integration of the stent into the patient-specific vasculature.* To place the designed FD into the digital vasculature, the following was carried out:
   a. A vessel wall was generated by digitally subtracting the patient-specific aneurysm and the vessel lumen from an enlarged copy of it.
   b. The vessel wall and the designed stent were cut in half tangentially to the vessel centerline.
   c. The part of the stent that intersected with the aneurysm was merged into the vessel wall, while the other part was discarded. As a result, the stent covered the orifice of the aneurysm (Figure, step 4).
   d. The aneurysm model was printed in two parts, the aneurysm sac with a stent and the remaining adjacent vasculature, so that the printing material did not solidify between the stent wires and to enable visual access to the stent. To facilitate assembly of the aneurysm model, rods and holes were added to the model within the cutting plane.

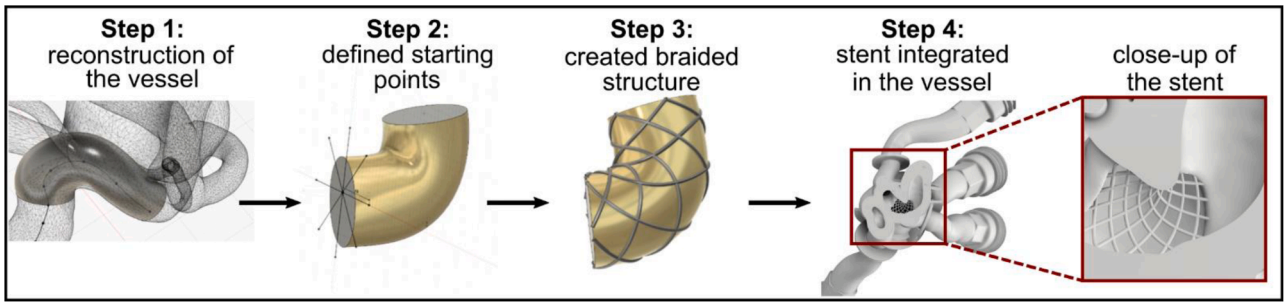

Fig. 2. Workflow to design 3D-printed flow-diverting stents (FD) in patient-specific aneurysm models. The vessel adjacent to the aneurysm is reconstructed along a centerline that follows the course of the healthy, unaffected vessel (step 1). Points were placed equidistantly on the 2D cross-section of the reconstructed vessel to mark the beginnings of the wires needed to create the braided stent structure (Step 2). The wires were wrapped helically around the vessel, alternating clockwise and counterclockwise from these points (Step 3). To digitally integrate the designed stent into the vasculature model, both were cut in half tangentially, so that the stent only covered the orifice of the aneurysm (Step 4).

A detailed manual of the developed manufacturing pipeline for 3D-printed FDs is freely available on Zenodo (https://doi.org/10.5281/zenodo.14987035).

2.5.3. Fabrication of aneurysm models

Before 3D printing, all digital models were equipped with markers perpendicular to the parental vessel or aneurysm to ensure that the MRI and post-processing workflow could be reproduced.

To evaluate the flow reduction in the aneurysm by the 3D-printed FDs and to compare them with commercial FDs, two empty aneurysm models were 3D printed. One model (**M1-empty**) remained empty to assess aneurysmal flow before treatment, while a commercial stent was inserted in the other model (**M2-commercial**) under X-ray control by trained medical personnel (DERIVO Embolisation Device, ACANDIS GmbH, Pforzheim, Germany).

Next, three aneurysm models with incorporated FDs were 3D printed. For this, a wire diameter of 0.25 mm was selected; to achieve different porosity values, the number of wires per model was varied: **M3-printed-20** contained 20 wires, **M4-printed-16** contained 16 wires, and **M5-printed-6** contained 6 wires.

For MRI, all models are placed in containers filled with a 3 % (weight) agarose gel solution, thus enhancing the overall MR signal and eliminating artifacts at air-tissue interfaces.

2.5.4. Determination of the porosity of the 3D-printed flow-diverting stents

The 3D-printed FD images were taken with a microscope camera to determine the physical porosity and wire diameter. The known diameter ($d = 1$ mm) of the 3D-printed rods (Supplementary Material, Section S.1.3, Figure S.3A) was used as the conversion factor between pixels and millimeters. The wire diameter was manually measured five times and averaged. To determine the porosity, first, the area covered by the mesh was delineated by polygonal line fitting. By creating a binary mask of the defined region of interest, the area of the mesh visible in the images was calculated. For each hole, the area was measured in a similar manner and summed up to obtain the total area of all open structures (Supplementary Material, Section S.1.3, Figure S.3B). The porosity was then calculated by dividing the area of the holes by the total stent area.

The measurement procedure was repeated five times to obtain a mean value and standard deviation of the mesh porosity. Image processing and all further calculations were performed using MATLAB.

To determine the CAD porosity, volume rendering of the models was aligned in the same way as the microscope camera images and snapshots were taken in the 3D modelling platform used (Fusion360, Autodesk, Inc., Mill Valles, California, USA). We estimated the porosity of the digital models using the same processing steps as described above.

2.6. In vitro MR imaging acquisition

To evaluate the flow in the aneurysm models, MRI was performed on a clinical 3 T MR system equipped with a 32-channel head coil (Ingenia CX, R5 V6.1, Philips Healthcare, Best, Netherlands). The aneurysm models were integrated into the flow pump setup and supplied with a flow rate of 4.2 ml/s at a constant time period of 0.8 s to match the physiological flow rates observed in the internal carotid arteries [30] (PD-1100, BDC Laboratories, Wheat Ridge, Colorado, USA). The set flow was controlled with the flow sensor (ME8-PXL, Transonic Systems Inc., Ithaca, New York, USA) at the inlet of the aneurysm model.

The water/glycerol mixture used was enriched with a gadolinium-based contrast agent to enhance the MR signal (0.33 ml/l Gadovist® 1.0 mmol/ml, Gadobutrol, Bayer Vital GmbH, Leverkusen, Germany).

The MRI protocol (Table 2) for each model included the following sequences:

1. *Time-of-flight (TOF) MRI* was used for geometric planning of subsequent sequences.
2. *2D phase-contrast (2D* PC*) MRI* was used to estimate the maximum velocity in the aneurysm and parental vessel. Several 2D PC sequences were recorded with different velocity-encoding parameters (venc) to determine the optimum venc value, which was approximately 10 % higher than the maximum observed velocity.
3. *4D flow MRI* [35–38] was used to measure velocities within the 3D imaging volume of the whole aneurysm model. Velocities observed in the aneurysm differed from those in the parental vessel. Therefore, two 4D flow MRI sequences were performed with different venc values optimized for velocities either in the aneurysm or in the

Table 2
Magnetic resonance imaging protocols used for flow experiments with aneurysm models (M1-M4).

	TOF	2D PC	4D Flow
Sequence type	3D T1 w GRE	3D PC GRE	3D PC T1 w GRE
Turbo factor		2	1
Acceleration technique	CS-SENSE	CS-SENSE	CS-SENSE
Acceleration factor	4.7	2.5	4.5
FOV [mm^3]	200 × 200 × 160	200 × 200 × 2	110 × 100 × 40.125
Acquired voxel [mm^3]	0.5 × 0.5 × 0.5	0.5 × 0.5 × 2	0.75 × 0.75 × 0.75
TE/TR [ms]	5.8/25	7.1/11	5.0/8.3
FA [°]	20	10	8
Cardiac frames		20	20
Scan time [min]	17:49	03:12	26:05

T1 w – T1-weighted, GRE – gradient echo, FOV – field of view, TE – echo time, TR – repetition time, FA – flip angle, CS-SENSE – compressed sensing-sensitivity encoding.

parental vessel. Specifically, venc values of 80 cm/s (M1-empty), 100 cm/s (M2-commercial), and 50 cm/s (M4-printed-16/M5-printed-6) were used to acquire the velocities in the parental vessel, while venc values of 55 cm/s (M1-empty), 20 cm/s (M2-commercial), 5 cm/s (M4-printed-16), and 25 cm/s (M5-printed-6) were selected to minimize velocity noise in the aneurysm sac. 4D flow MRI datasets are available on Zenodo (https://doi.org/10.5281/zenodo.14981710).

2.7. In vitro MR imaging post-processing

The magnitude and three phase datasets (x,y,z) per acquired 4D flow sequence were reconstructed on the MRI system. The 4D flow MRI data were post-processed according to the 4D flow consensus statement [39, 40] (GTFlow 3.2.13, GyroTools LLC, Zurich, Switzerland), including the following steps:

1. *Linear phase correction.* To correct for eddy currents, a linear phase correction was performed by fitting a linear phase offset to the phase values of static tissue voxels and subsequently subtracting from all voxels.
2. *Segmentation.* Data from the vessel lumen are required exclusively to quantify the flow. Therefore, it is necessary to separate the inner vessel lumen and the 3D-printed vessel wall. The 3D segmentation of the vessel was achieved by 1) applying a magnitude image intensity mask, 2) manual masking of the vessel geometry in each acquired slice, and 3) unmasking voxels in the aneurysm or vessel that were still masked due to the previously defined intensity threshold.
3. *Velocity anti-aliasing.* Each time frame of the phase images was optically inspected for the presence of phase aliasing in the entire vessel and aneurysm sac. None was detected.
4. *Quantification.* Equidistant 2D cross-sectional planes ($z = 1$ mm) were placed in the parental vessel (Fig. 3A, section 1 and section 2, $n = 5$) and the entire aneurysm sac ($n = 10$). A circular region of interest was created by delineating the inner vessel or aneurysm surface in each cross-section. The flow and velocity values were spatially averaged within this region. Next, for each section of the parental vessel or aneurysm sac, flow and velocities were averaged among five or ten planes, respectively, resulting in a time-dependent curve per section (Fig. 3B). In addition, the standard deviation was calculated for the two sections of the parental vessel.

3. Results

3.1. Physical porosity of the 3D-printed meshes

Meshes with CAD wire diameters of 0.05 mm to 0.5 mm and CAD porosities between 30 % and 80 % exhibited cavity structures (Table 3). Meshes with an intended CAD porosity of 10 % were blocked entirely after 3D printing (Fig. 4). With decreasing wire diameter, this blockage was present with decreasing porosity. At the thinnest wire diameter of 0.05 mm, only the mesh with a CAD porosity of 80 % had cavities. All blocked meshes were excluded from further analysis (Supplementary Material, Section S.2.1, Figure S.4).

The resulting physical porosity of open meshes ranged between 14 % and 54 % (Table 3). Porosities were around two-thirds smaller than the CAD values. Deviations from the CAD porosities were greater for meshes with smaller wire diameters, 0.05 mm, and 0.1 mm. In addition, the physical wire diameter determined for these meshes was up to twice as large as the digital wire diameter. Physical wire diameters of 0.25 mm were on the same order of magnitude as the CAD values. This resulted in cell lengths between 0.23 mm and 2.14 mm.

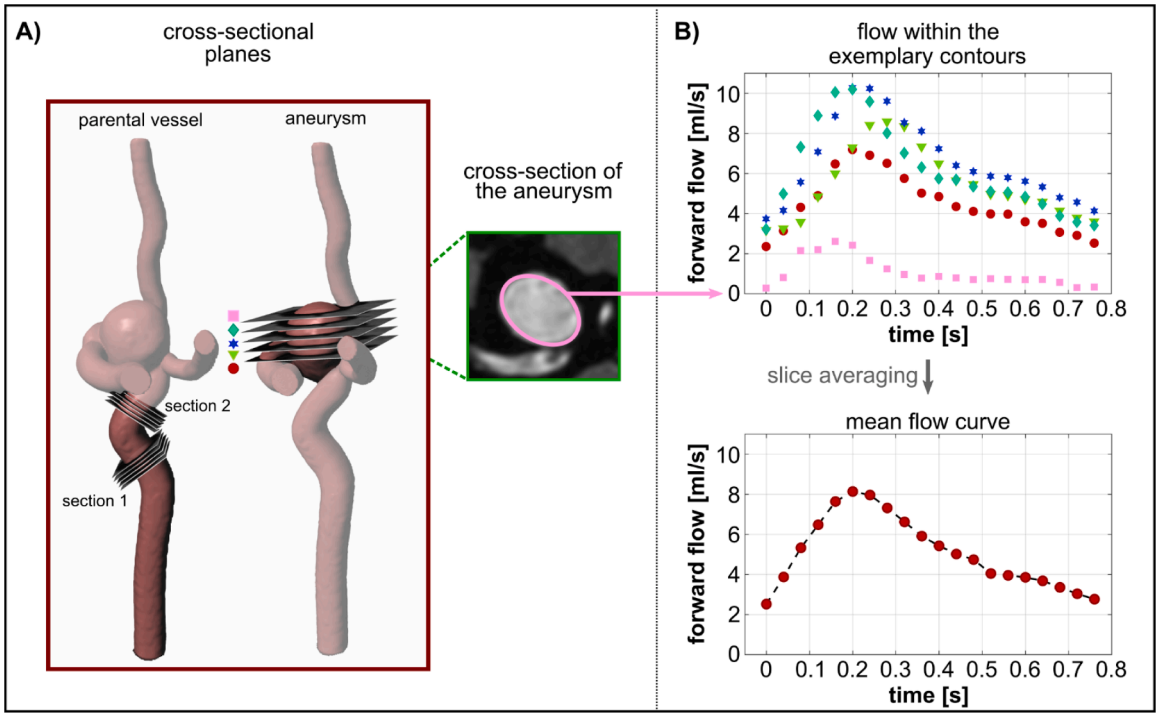

Fig. 3. Post-processing steps of the 4D flow MRI data of the patient-specific aneurysm models. A) 2D cross-sectional planes were placed equidistantly ($z = 1$ mm) in two parts of the parental vessel (section 1 and section 2) and the entire aneurysm sac (evaluated planes with $z = 1$ mm; here, only every second plane is shown exemplarily). Flow and velocity within the vessel or aneurysm were determined by delineating the inner vessel contour. B) A time-dependent flow curve was obtained for each drawn contour. Averaging the contours of each region within the model yielded a mean flow curve per section in the parental vessel and aneurysm sac. In each plane, a contour delineating the vasculature was manually drawn. Flow and velocity were spatially averaged within each contour and each plane for each section, resulting in one time-dependent flow curve per section.

Table 3
CAD values and apparent physical values of the wire diameter, the porosity, and the square cell length of the 3D-printed meshes. The apparent physical design parameters were determined in images of the meshes captured by the video microscope camera.

Wire diameter [mm]		Porosity [%]		Square cell length [mm]	
CAD	physical	CAD	physical	CAD	physical
0.05	0.11 ± 0.01	80	32	0.47	0.30 ± 0.04
	0.18 ± 0.01	60	21	0.44	0.24 ± 0.04
0.1	0.20 ± 0.01	70	36	0.61	0.41 ± 0.04
	0.18 ± 0.02	80	48	0.95	0.70 ± 0.04
	0.26 ± 0.02	30	14	0.55	0.23 ± 0.03
	0.23 ± 0.01	50	33	0.85	0.55 ± 0.05
0.25	0.24 ± 0.02	60	39	1.11	0.80 ± 0.03
	0.26 ± 0.01	70	50	1.53	1.12 ± 0.03
	0.22 ± 0.02	80	51	2.37	1.90 ± 0.06
	0.48 ± 0.02	30	20	1.11	0.53 ± 0.04
	0.45 ± 0.04	50	37	1.71	1.06 ± 0.04
0.5	0.43 ± 0.02	60	39	2.22	1.59 ± 0.04
	0.48 ± 0.03	70	54	3.06	2.14 ± 0.10
	0.43 ± 0.06	80	54	4.74	2.13 ± 0.09

3.2. Permeability of the mesh

All tested meshes reduced the flow through the bottle cap compared to the bottle cap without a mesh (Fig. 5). Additionally, the flow through the mesh increased with porosity (slope = 0.33), showing a strong correlation ($\rho = 0.86$ and p-value = 0.00005).

Wire diameters of 0.1 mm, 0.25 mm, and 0.5 mm individually showed a linear relationship between flow and porosity with calculated slopes of 0.59, 0.59, and 0.52, respectively. The corresponding correlation coefficients were 1, 0.99, and 0.98 ($p = 0.03$, 0.0006 and 0.002).

Despite similar porosity values, the flow rate was different for different wire diameters. For example, at a 20 % and 21 % porosity, the difference in the median flow rate for wire diameters of 0.1 mm and 0.5 mm was 1.5 ml/s. The same applies to a 48 % and 50 % porosity with wire diameters of 0.1 mm and 0.25 mm, respectively, with a difference in the median flow rate of 2.7 ml/s (Supplementary Material, Section S.2.2, Table S.1).

Additionally, the meshes reduced flow under all supplied pulsatile flow rates, with higher porosity again resulting in increased flow through the mesh (Supplementary Material, Section S.2.3, Figure S.5, Table S.2).

3.3. Apparent porosity of the 3D-printed flow-diverting stents

All fabricated models with embedded FDs exhibited cavity structures after 3D printing (Fig. 6). The measured wire diameter was smaller than the intended CAD value of 0.25 mm with mean values of 0.18 mm (SD = ± 0.01 mm), 0.2 mm (SD = ± 0.01 mm) and 0.17 mm (SD = ± 0.02 mm) for the FD models containing 20, 16, and 6 wires. In the images of the digital models, the mean values of the wire diameter were measured as 0.13 mm (SD = ± 0.02 mm), 0.15 mm (SD = ± 0.02 mm), and 0.18 mm (SD = ± 0.02 mm) for the corresponding FD models (Supplementary Material, Section S.2.4, Table S.3).

The wire diameter determined in the digital models deviates from the intended CAD value. Therefore, the accuracy of the measuring method was limited and an additional systematic error of 0.1 mm must be considered.

The apparent porosities in the 3D-printed models were determined to be 26 % (SD = ±0 %), 32 % (SD = ±2 %), and 74 % (SD = ±1 %) for the FD models containing 20, 16, and 6 wires, respectively. The CAD porosity in the corresponding digital models was 47 % (SD = ±2 %), 53 % (SD = ±2 %), and 79 % (SD = ±1 %), respectively (Supplementary Material, Section S.2.4, Table S.3).

3.4. In vitro MR imaging flow evaluation

MR flow imaging and further evaluation was feasible for four of the five aneurysm models produced (M1-empty, M2-commercial, M4-printed-16, and M5-printed-6): ToF MRI of the model with an inserted FD and a determined physical porosity of 26 % (M3-printed-20) showed residual bubbles in the aneurysm sac; therefore, no 4D flow MRI was performed (Supplementary Material, Section S.2.5, Figure S.6).

For all remaining models, the flow was similar in section 1 of the parental vessel (Fig. 7). Here, some differences in the flow curves were observed, but mean flow values were 3.9 ± 1.3 ml/s for M1-empty, 3.9 ±

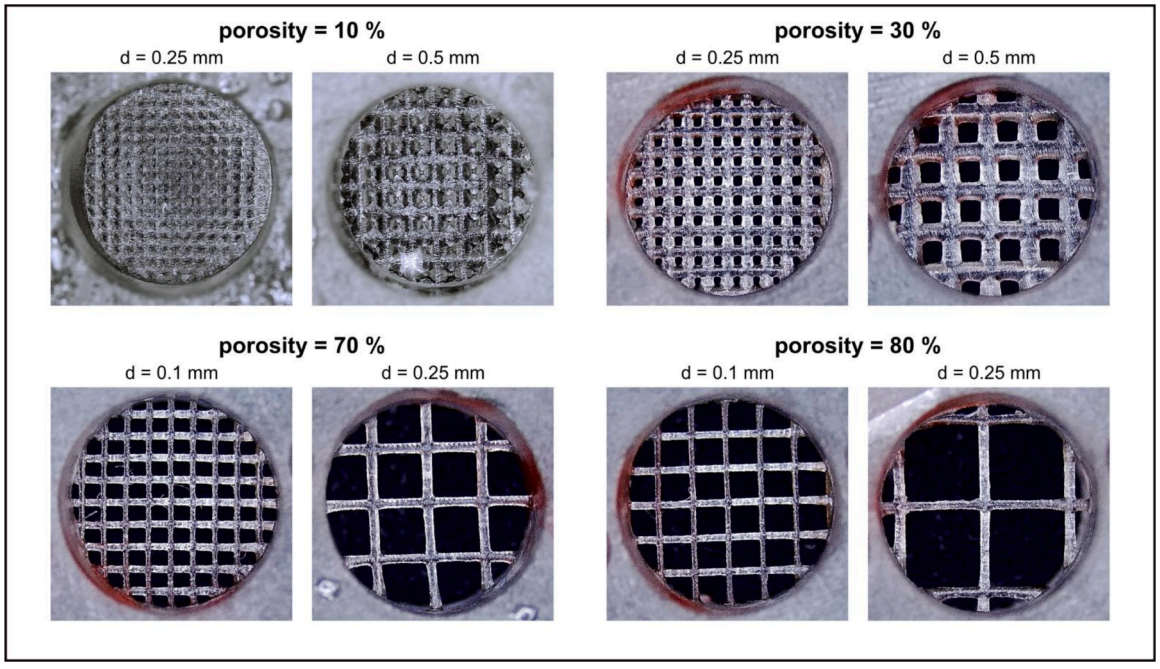

Fig. 4. Exemplary microscope camera images of the 3D-printed meshes with intended porosities of 10 %, 30 %, 70 %, and 80 % and related wire diameters of 0.25 mm and 0.5 mm or 0.1 mm and 0.25 mm.

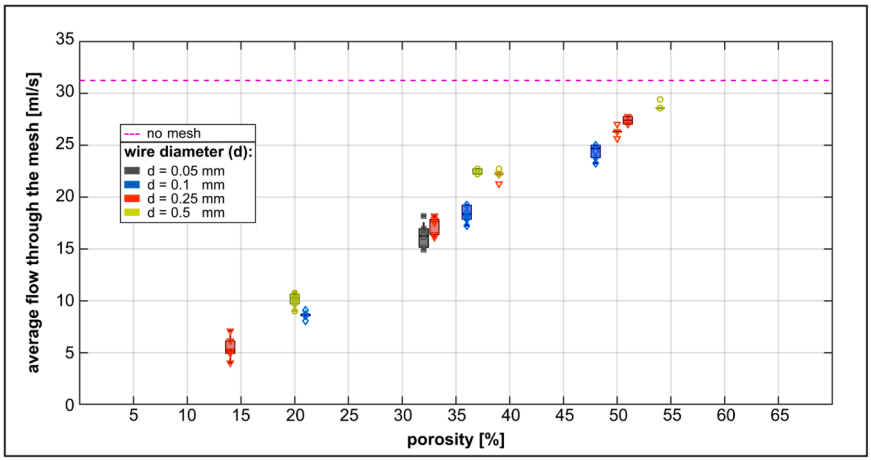

Fig. 5. Gravity-induced average flow through the mesh measured six times (markers) and the resulting median value (box plot). The flow through the mesh is directly proportional to the porosity (slope = 0.33 with a correlation coefficient of 0.86 ($p = 0.00005$).

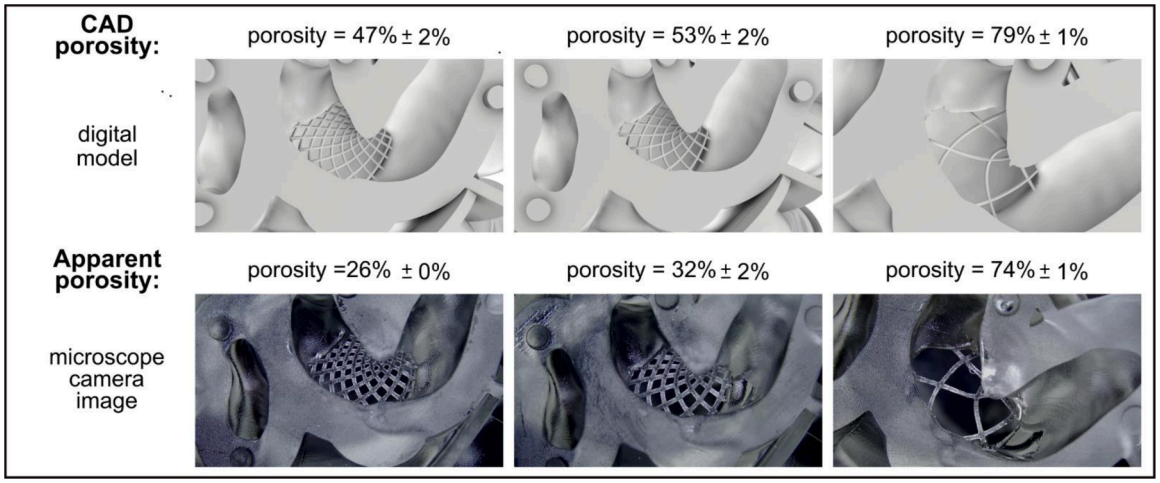

Fig. 6. Snapshots of the digital models (top) in matched orientation to the corresponding microscope camera images of the 3D-printed FDs (bottom).

1.4 ml/s for M2-commercial, 3.6 ± 0.5 ml/s for M4-printed-16, and 3.5 ± 1.1 ml/s for M5-printed-6. In section 2 of the parental vessel, the flow curves were similar among M1-empty, M4-printed-16, and M5-printed-6 and mean values were equal, at 3.6 ± 1.1 ml/s, 3.5 ± 0.5 ml/s, and 3.5 ± 1.1 ml/s, respectively, while M2-commercial exhibited a much lower mean flow rate of 1.8 ± 0.6 ml/s. The flow evaluation planes of section 2 intersected with the location of the commercial FD, which caused stent-induced shielding artifacts [22]. The latter affects the near-stent flow assessment and led to an apparent flow reduction.

The aneurysmal mean flow was 5.1 ± 1.8 ml/s in M1-empty. All types of FD stents investigated reduced the flow in the aneurysm. The 3D-printed FD with an apparent porosity of 32 % (M4-printed-16) reduced the flow more effectively with a mean flow rate of 0.3 ± 0.02 ml/s than the 3D-printed FD with an apparent porosity of 74 % (M5-printed-6) with a mean flow of 1.0 ± 0.2 ml/s. Flow reduction was lowest for the commercial FD (M2-commercial) with a mean flow of 1.2 ± 0.3 ml/s. This resulted in flow reductions of 94 % for M4-printed-16, 76 % for M5-printed-6, and 65 % for M2-commercial (Supplementary Material, Section S.2.6, Table S.4).

4. Discussion

In this work, we demonstrated that 3D-printed meshes can effectively reduce and divert flow. First, we tested the general permeability of the meshes under gravity conditions, then under pulsatile flow conditions. Finally, we develop a protocol to insert the meshes into the aneurysm models and compared their flow-reducing properties with those of commercial FDs using 4D flow MRI.

4.1. Workflow for the design of aneurysm models with 3D-printed flow-diverting stents

The design of 3D-printed FDs starts by selecting an aneurysm case suitable for treatment with FDs. Then, the patient's vasculature is segmented, refined, and simplified by considering only the vessel branches relevant for aneurysm treatment. This part was adopted from our previous work [31].

Once the 3D-segmented vasculature was available, the next crucial step was to reconstruct the healthy segment of the vessel. We decided to create a cross-section of about 1–2 cm before and after the aneurysm and connect these cross-sections with a centerline. The centerline was created manually, rendering is a subjective decision in the protocol. Automatically generating the centerline would make the protocol more user-independent; for example, it has already been shown that algorithms based on deep learning can do this [41]. In the future, it would be beneficial to consult a physician about each aneurysm case to understand how far from the aneurysm that physician would start placing the stent and where it would end. To design a stent around the centerline, a vessel surface in the healthy segments of the vasculature was again manually outlined with a spline. Here, too, automated approaches to

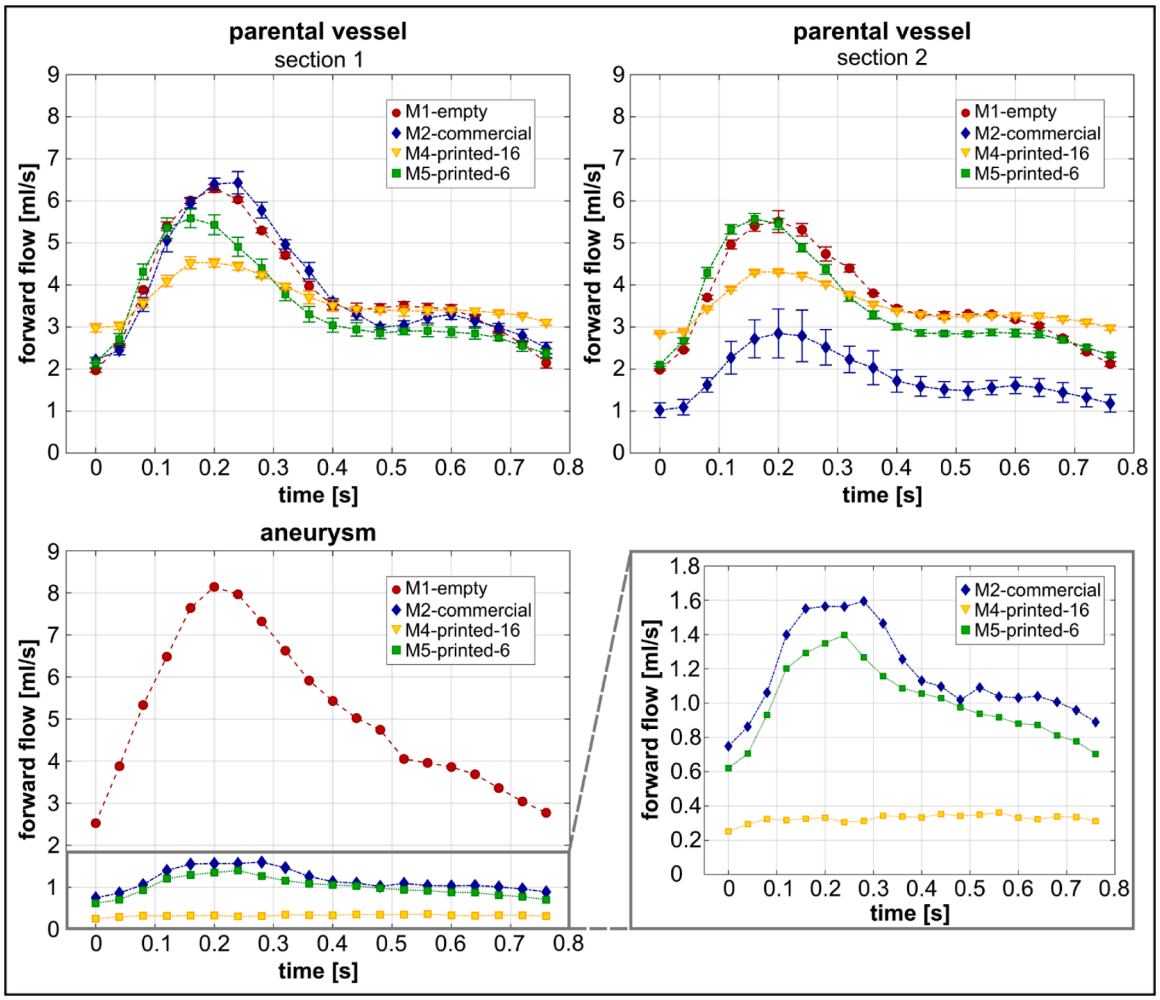

Fig. 7. Mean flow curves for each 3D-printed vasculature model examined, *i.e.*, an empty reference model (red circles, M1-empty), a model with an inserted commercial FD (blue diamonds, M2-commercial), and the 3D-printed FD models with physical porosities of 32 % (yellow triangles, M4-printed-16) and 74 % (green squares, M5-printed-6). In the parental vessel far from the flow-diverting device (section 1), all models showed a similar flow profile and mean flow. Near the FDs (section 2), metal artifacts caused by the commercial device led to an apparent decrease in flow, whereas this did not occur for the 3D-printed stents. Within the aneurysm, all FDs achieved the intended flow reduction; notably, the 3D-printed FD with 74 % porosity and the commercial FD showed a similar flow reduction.

outline the surface would make the protocol more robust. Next, to create the 3D-printed stent, one should decide on the number of wires and the wire thickness. After that, the wires are automatically wrapped around the vessel segment based on these parameters and the reconstructed healthy vessel segments.

The protocol was demonstrated and evaluated according to the geometry of one patient-specific aneurysm, but the steps described can be applied to any aneurysm suitable for FD treatment. The protocol is straightforward and can be completed relatively quickly. The initial aneurysm model takes about 6–8 h to produce, and only 2–3 h are needed to further implement the 3D-printed FDs. Once the 3D model of the FD is created, stent porosity and wire diameter can be easily adjusted, whereby the most time-consuming step is redefining the wire starting points.

4.2. 3D printing

Here we used a SLA 3D printer to produce vascular models. This particular SLA printer is an affordable mid-range printer, more expensive than other printer technologies such as material extrusion, but much cheaper than Polyjet [42,43]. Moreover, SLA offers a smooth surface of the printed models and high printing accuracy with a minimum layer thickness and in-plane resolution of 0.025 mm each. The aneurysm models produced with the SLA 3D printer gave an accurate representation of the vessel lumen and aneurysm sac [31]; thus, we decided to use the same technology for the 3D printing of stents.

The wire thickness of commercial FDs is about 0.03 mm [44]. The resolution of the available 3D printer is on the same order of magnitude, making it challenging to produce the 3D-printed stents with the same wire diameters as commercial FDs. However, it has been previously reported that one of the most important design parameters for FDs is porosity [32]. Smaller porosities seem to divert flow from the aneurysm more effectively [25]. Therefore, we decided to test whether a porosity range equivalent to that reported for commercial FDs can be achieved using the SLA printer.

To do this, we designed and 3D printed simplified mesh-like structures to determine the limits of the 3D printing process. The designed holes and wire thicknesses ranged from 0.07 mm to 4.74 mm and 0.05 mm to 0.5 mm, respectively. However, after 3D printing, the holes smaller than 0.44 mm were blocked, and wire diameters smaller than 0.05 mm were unstable and did not cover the entire mesh (Supplementary Material, Section S.2.1, Figure S.4). Nevertheless, 3D-printed permeable meshes with wire diameters between 0.11 mm and 0.48 mm and holes between 0.23 mm and 2.14 mm were obtained (Table 3). In this study, wire diameters two times larger than the layer thickness of the 3D printer could be printed with a set CAD value of 0.05 mm.

However, the wire diameter with a CAD value of 0.25 mm was the one produced most accurately. Therefore, we decided to use this wire diameter to produce the 3D-printed stents.

The simple meshes we designed aimed to cover a porosity range of between 30 % and 80 %, but due to the limitations of 3D printing, we only achieved a porosity range of 14 % to 54 %. Higher porosities could not be realized with the current simple mesh design, as the originally planned opening with inner diameter of 6 mm was too small. A further increase in porosity could not be distinguished as the mesh with a porosity of 80 % only contains two perpendicular wires in the center of the opening (Supplementary Material, Section S.1.2, Figure S.2). However, this size was chosen because about 80 % of the detected aneurysms have a maximum size < 10 mm [45] and endovascular treatment is approved for wide-neck aneurysms with a diameter ≥ 4 mm [8]. Still, in our tests of the permeability of the meshes under gravity conditions, we were able to demonstrate a linear dependence between porosity and flow reduction.

To achieve precisely printed meshes with smaller wire diameters and openings, polymeric and metallic microstructures can be fabricated with a sub-100 nm resolution by applying micro-/nano 3D printing technologies. Those printers are capable of printing a small model volume in the micrometer range [46], which is perfect for printing FDs, but not sufficient to produce an entire aneurysm model. With the SLA printer used here, aneurysm models with a maximum size of $145 \times 145 \times 185$ mm can be printed allowing to fit aneurysms and adjacent vasculature. A combination of several printing technologies, one to print stents and another to print the aneurysm models, can potentially be used to meet the requirements for the wire size. Alternatively, an aneurysm model can be scaled up to match the size ratio between commercial and human vasculature with that of the 3D-printed and aneurysm models. The fluid dynamic similarity parameters such as Reynolds and Womersley numbers must be matched between scaled-up and real-size systems.

4.3. Evaluation of flow effects with 3D-printed meshes

Aneurysm models containing 3D-printed FDs were printed with porosities of 26 %, 32 %, and 74 %. Thus, the fabrication of 3D-printed replicas of FDs is possible within the order of magnitude of commercial FD porosities [8,25]. The selected aneurysm has a neck diameter of 9 mm, which made it possible to incorporate higher porosities and keep the same wire diameter. The porosity was controlled by varying the number of wires.

The 3D-printed stent with an apparent porosity of 74 % reduced the flow in the same way as the commercial FD investigated in our study, at 76 % and 65 %, respectively. Our findings are consistent with previous research, where the flow reduction of commercial FDs ranged from 19 to 80 % [47,48]

The 3D-printed FDs with a porosity of 26 % resulted in zero flow within the aneurysm, making it impossible to remove the air bubbles in the aneurysm sac. In the preliminary tests, the meshes with this porosities were permeable. The difference between flow changes in the aneurysm model and other tests can likely be attributed to the angle at which the flow faces the mesh. In the preliminary test, the flow was parallel to the mesh holes, while in the aneurysm it was under a 100° inflow angle. The inflow angle is the defined angle between flow in the parental vessel and the aneurysm dome axis. Lower peak flow velocities are related to smaller inflow angles [49]. As a result, better treatment effects can likely be achieved. Berg et al. showed that patients with smaller intra-aneurysmal flow before treatment presented with a complete aneurysm occlusion at the 1-year follow-up, while others required retreatment [48] Indeed, it was shown that an inflow angle of >90° was associated with incomplete aneurysm occlusion at 1-year follow-up [50]. Moreover, larger inflow angles were associated with a larger aneurysm size, lower wall shear stress, and a higher aneurysm vessel wall enhancement grade [51]. These parameters are associated with an increased aneurysm rupture risk [52].

Although the perpendicular orientation of the mesh to the flow in the preliminary test does not fully replicate the *in vivo* scenario, this simple test allowed us to effectively narrow down the porosities to be tested. If a mesh proves impermeable under the gravity or pulsatile conditions in perpendicular orientation, it will also remain impermeable in the aneurysm model, streamlining the testing process and focusing efforts on more promising configurations. Still, a non-perpendicular orientation of the stent to the flow in the preliminary test should also be considered in future work.

4.4. Applicability of 3D-printed stents

Our 3D-printed FD stents are currently suitable for testing and optimizing the stent design parameters, *e.g.*, porosity and stent efficiency of the same porosity in different aneurysm geometries. Moreover, the effect of flow modulation can be investigated by applying *in vivo* methods, such as 4D flow MRI. Investigation of the stent design with *in vivo* methods will facilitate the transition from *in silico* and *in vitro* trials to *in vivo* scenarios.

Furthermore, the data obtained from 3D-printed stents are free of metal artifacts, which often originate from commercial metal implants. In some cases, metal artifacts prevent any flow assessment in the aneurysm, especially in small aneurysms [24]. In our study, the commercial FD showed a significant reduction in flow within the parent vessel at the junction with the FD, while the 3D-printed FDs did not alter the velocity in the parent vessel. This discrepancy is not due to the flow-diverting properties of the commercial stents, but rather the metal-induced artifacts on MR imaging, which impact the accuracy of velocity measurements in the parent vessel [21]. It has been previously reported that FDs could shield the imaging volume inside the stent, resulting in a different magnetic field and thus a change in measured flow [22]. Therefore, the use of 3D-printed stents could be beneficial for verifying and validating the velocity measurements of new MRI sequences as well as for numerical simulations. In the past, 3D-printed structures have been used to validate CFD using MRI and fabricated coronary stents [23].

The 3D-printed FDs proposed here are not intended for clinical treatment yet. The stents were integrated with the aneurysm geometry during the digital design phase and then 3D printed as a single unit. The material currently used for 3D printing is rigid, which prevents realistic compression of the FD and, therefore, does not allow for practical deployment in patients. Moreover, the rigid material used for 3D printing does not mimic the mechanical properties of clinically used FDs, such as flexibility and fatigue resistance, which are crucial for the stent's performance within the dynamic vascular environment.

Additionally, the performance of FDs is influenced by the deployed porosity, pore density, and wall apposition, all of which can vary significantly depending on the deployment procedure and the specific anatomical context. In our study, deployment was performed virtually, achieving perfect wall opposition—a scenario that is difficult to replicate *in vivo* due to the inherent complexities of vascular anatomy, such as vessel curvature, calcifications, and other factors that affect how the stent conforms to the vessel wall.

Our ultimate goal is to develop a platform that allows for the efficient optimization of FD designs before moving to clinical-grade manufacturing and *in vivo* testing. Despite the current limitations, the methods presented here is already can be used to investigate the influence of stent design parameters on treatment outcome using *in vivo* methods.

While this study focuses on the rapid prototyping of FD designs for preclinical testing and optimization, future work could explore the use of more flexible, biocompatible materials for 3D printing. The possibility of 3D printing patient-specific bifurcation stents with shape memory polymers has already been demonstrated [53]. The resulting stents were quite thick for actual treatment but could still be compressed and navigated into the bifurcation in the silicone vascular model. In another

study, the authors investigated 3D-printed biodegradable stents for biliary strictures and demonstrated their efficiency *in vivo* in a porcine model [54].

Overall, we anticipate that advances in 3D printing technologies, particularly direct metal laser printing with shape memory materials [55], will revolutionize conventional FD fabrication. In areas such as orthopedics, patient-specific implants fabricated using 3D printing have shown benefits in terms of implant-bone alignment and patient outcomes [56]. In addition, stents produced using various 3D printing technologies are considered to have great potential for cardiovascular treatment [57]. By using micro-extrusion technology and a newly developed mini-screw extruder, Wang et al. designed filament-based cardiovascular stents with different shapes and geometric structures [58]. Xiao et al. utilized micro-stereolithographic 3D printing and metal thin-film deposit for direct 3D printing of thin-walled cardiovascular stents made of mechanical metamaterials [59]. We envision that 3D printing technologies will soon be applicable in the field of endovascular treatment.

4.5. Limitations

Our study has several limitations. First, the design protocol was evaluated using only one aneurysm geometry; however, we anticipate no substantial challenges in adapting it to other geometries. A limited range of stent porosities was tested, though the 74 % porosity showed similar flow reduction to the commercial FD. We only compared our 3D-printed FDs to one commercial FD, specifically the most used in our department, despite variability in flow-reducing efficiency among different manufacturers. The 3D printer used could not fabricate wire sizes comparable to those of commercial stents, although porosity was maintained. The limited printing resolution led to deviations from the designed models, particularly in smaller structures, such as larger printed wire diameters, rounded corners, and resin-filled holes. Therefore, the apparent FD stent porosity should always be calculated after 3D printing. The image processing methods to calculate mesh porosity were also prone to errors due to threshold-based pixel detection and manual measurements. To address this, future work should consider using imaging modalities that provide true 3D geometry, like micro-computed tomography, and automated methods for stent property determination. Additionally, the flow rates were set to match physiological values observed in the internal carotid artery, leading to a lack of fluid dynamic similarity between the commercial and 3D-printed FDs. This decision was because the characteristic distance (aneurysm model size) remained unchanged. Ideally, scaling up the aneurysm model with 3D printed FDs would allow for a comparable size ratio between the aneurysm and wire diameters. Then, by adjusting the fluid properties to match the Reynolds and Womersley numbers, one can ensure fluid dynamic similarity between the scaled-up models and commercial stents, leading to more accurate comparisons.

5. Conclusion

Using the workflow presented here, 3D-printed FDs can be produced to optimize and test their design parameters. The resulting 3D-printed stents reduced flow as efficiently as commercial FD stents. In addition, the 3D-printed FDs do not generate metal artifacts, making them a good tool for optimizing and verifying *in vivo* imaging methods, such as 4D flow MRI.

Data availability

A manual on the design of the 3D-printed FDs and stl files of the print-ready aneurysm models are available on Zenodo (https://doi.org/10.5281/zenodo.14987035). 4D flow MRI raw datasets are also available via the Zenodo repository (https://doi.org/10.5281/zenodo.14981710). Videos of the permeability test and data from the flow sensor will be provided by the corresponding author upon reasonable request.

Funding

This work was supported by the German Research Foundation (GRK2154: P2b), the Bruhn Foundation (2022), and Intramural Research Funding from the Faculty of Medicine at Kiel University (2024). MOIN CC was founded by a grant from the European Regional Development Fund (ERDF) and the Zukunftsprogramm Wirtschaft of Schleswig-Holstein (project no 122–09–053).

Author contributions

Conceptualization and design of the project: NL, MSP. Design and production of simplified 3D mesh models: LB, OAO, TS. Construction of the experimental setups for the mesh permeability and flow test: LB, OAO. Design and fabrication of the 3D aneurysm models: LB, OAO, MSP. Performing mesh permeability and flow test: LB, OAO, TS. Performing *in vitro* MRI: LB, OAO, MSP, HT. Data analysis and evaluation: LB, MSP. Data visualization: LB. Statistical analysis: LB. Supervision and funding acquisition: JBH, OJ, NL, MSP. Writing – original draft preparation: LB, MSP. Writing – review and editing: LB, JBH, OJ, NL, OAO, MSP, HT. All authors have read and approved the published version of the manuscript.

Competing interests

The author(s) declare the following potential conflicts of interest: NL has received fees for consulting and speaking from Balt International SAS, Acandis GmbH, Stryker Corporation.

Declaration of generative AI and AI-assisted technologies in the writing process

During the preparation of this work the author(s) used ChatGPT (OpenAI) in order to improve language and readability of the manuscript. After using this tool/service, the author(s) reviewed and edited the content as needed and take(s) full responsibility for the content of the publication.

Declaration of competing interest

The authors declare the following financial interests/personal relationships which may be considered as potential competing interests:

The author(s) declare the following potential conflicts of interest: NL has received fees for consulting and speaking from Balt International, SAS, Acandis GmbH, Stryker Corporation.

Acknowledgements

We gratefully acknowledge the continued research support by Philips Healthcare, Germany, Hamburg. We thank Acandis for providing the DERIVO device for *in vitro* testing. We acknowledge support by Kiel University and the Medical Faculty for supporting the Molecular Imaging North Competence Center (MOIN CC) as core facility for imaging *in vivo*. OAO was participating in this research study during her internship in our group in 2022 granted by the DAAD RISE Germany program.

Supplementary materials

Supplementary material associated with this article can be found, in the online version, at doi:10.1016/j.stlm.2025.100196.

References

[1] Hackenberg KAM, Hänggi D, Etminan N. Unruptured intracranial aneurysms: contemporary data and management. Stroke 2018;49:2268–75.
[2] Ortiz AFH, Suriano ES, Eltawil Y, et al. Prevalence and risk factors of unruptured intracranial aneurysms in ischemic stroke patients – A global meta-analysis. Surg Neurol Int 2023;14:222.
[3] Brisman JL, Song JK, Newell DW. Cerebral aneurysms. N Engl J Med 2006;355:928–39.
[4] Lee KS, Zhang JJY, Nguyen V, et al. The evolution of intracranial aneurysm treatment techniques and future directions. Neurosurg Rev 2022;45:1–25.
[5] Briganti F, Leone G, Marseglia M, et al. p64 Flow Modulation Device in the treatment of intracranial aneurysms: initial experience and technical aspects. J NeuroInterventional Surg 2016;8:173–80.
[6] Tähtinen OI, Manninen HI, Vanninen RL, et al. The silk flow-diverting stent in the endovascular treatment of complex intracranial aneurysms: technical aspects and midterm results in 24 consecutive patients. Neurosurgery 2012;70:617–24.
[7] Kraus B, Goertz L, Turowski B, et al. Safety and efficacy of the Derivo Embolization Device for the treatment of unruptured intracranial aneurysms: a multicentric study. J NeuroInterventional Surg 2019;11:68–73.
[8] Maragkos GA, Dmytriw AA, Salem MM, et al. Overview of different flow diverters and flow dynamics. Neurosurgery 2020;86:S21–34.
[9] D'Urso PI, Lanzino G, Cloft HJ, et al. Flow diversion for intracranial aneurysms: a review. Stroke 2011;42:2363–8.
[10] Yamada K, Imamura H, Ozaki S, et al. A review of current flow diverters. J Neuroendovascular Ther 2024. ra.2023-0078.
[11] Lylyk I, Scrivano E, Lundquist J, et al. Pipeline embolization devices for the treatment of intracranial aneurysms, single-center registry: long-term angiographic and clinical outcomes from 1000 aneurysms. Neurosurgery 2021;89:443–9.
[12] Khorasanizadeh M, Shutran M, Schirmer CM, et al. North American multicenter experience with the Flow Redirection Endoluminal Device in the treatment of intracranial aneurysms. J Neurosurg 2022:1–11.
[13] Kashkoush A, El-Abtah ME, Petitt JC, et al. Flow diversion for the treatment of intracranial bifurcation aneurysms: a systematic review and meta-analysis. J NeuroInterventional Surg 2023. jnis-2023-020582.
[14] Velvaluri P, Pravdivtseva MS, Lima de Miranda R, et al. Design characterization of thin film flow diverter stents (FDS) based on SMA's: FEA, CFD and MRI study. Shape Mem Superelasticity 2019. https://doi.org/10.1007/s40830-019-00223-8. Epub ahead of print 20 June.
[15] Zhang M, Anzai H, Chopard B, et al. Towards the patient-specific design of flow diverters made from helix-like wires: an optimization study. Biomed Eng OnLine 2016;15:159.
[16] Fu W, Gu Z, Meng X, et al. Numerical simulation of hemodynamics in stented internal carotid aneurysm based on patient-specific model. J Biomech 2010;43:1337–42.
[17] Janiga G, Daróczy L, Berg P, et al. An automatic CFD-based flow diverter optimization principle for patient-specific intracranial aneurysms. J Biomech 2015;48:3846–52.
[18] Berg P, Saalfeld S, Voß S, et al. A review on the reliability of hemodynamic modeling in intracranial aneurysms: why computational fluid dynamics alone cannot solve the equation. Neurosurg Focus 2019;47:E15.
[19] Janiga G, Rössl C, Skalej M, et al. Realistic virtual intracranial stenting and computational fluid dynamics for treatment analysis. J Biomech 2013;46:7–12.
[20] Velvaluri P, Pravdivtseva MS, Hensler J, et al. A realistic way to investigate the design, and mechanical properties of flow diverter stents. Expert Rev Med Devices 2021;18:569–79.
[21] Pereira VM, Brina O, Delattre BMA, et al. Assessment of intra-aneurysmal flow modification after flow diverter stent placement with four-dimensional flow MRI: a feasibility study. J NeuroInterventional Surg 2015;7:913–9.
[22] Bouillot P, Brina O, Delattre BMA, et al. Neurovascular stent artifacts in 3D-TOF and 3D-PCMRI: influence of stent design on flow measurement. Magn Reson Med 2019;81:560–72.
[23] Oldenburg J, Borowski F, Schmitz K-P, et al. MRV-validated numerical flow analysis of thrombotic potential of coronary stent designs. Curr Dir Biomed Eng 2019;5:77–80.
[24] Korte J, Gaidzik F, Larsen N, et al. *In vitro* and in silico assessment of flow modulation after deploying the Contour Neurovascular System in intracranial aneurysm models. J NeuroInterventional Surg 2023. jnis-2023-020403.
[25] Ravindran K, Casabella AM, Cebral J, et al. Mechanism of action and biology of flow diverters in the treatment of intracranial aneurysms. Neurosurgery 2020;86.S13–S19.
[26] Bradley D, Roth G. Adaptive thresholding using the integral image. J Graph Tools 2007;12:13–21.
[27] Otsu N. A threshold selection method from gray-level histograms. IEEE Trans Syst Man Cybern 1979;9:62–6.
[28] Segur JB, Oberstar HE. Viscosity of glycerol and its aqueous solutions. Ind Eng Chem 1951;43:2117–20.
[29] Shibeshi SS, Collins WE. The rheology of blood flow in a branched arterial system. Appl Rheol 2005;15:398–405.
[30] Zarrinkoob L, Ambarki K, Wåhlin A, et al. Blood flow distribution in cerebral arteries. J Cereb Blood Flow Metab 2015;35:648–54.
[31] Pravdivtseva MS, Peschke E, Lindner T, et al. 3D-printed, patient-specific intracranial aneurysm models: from clinical data to flow experiments with endovascular devices. Med Phys 2021;48:1469–84.
[32] Velvaluri P, Pravdivtseva MS, Berg P, et al. Thin-film patient-specific flow diverter stents for the treatment of intracranial aneurysms. Adv Mater Technol 2021;6:2100384.
[33] Adams R, Bischof L. Seeded region growing. IEEE Trans Pattern Anal Mach Intell 1994;16:641–7.
[34] Lorensen WE, Cline HE. Marching cubes: a high resolution 3D surface construction algorithm. In: Seminal graphics. New York, NY, USA: ACM; 1987. p. 347–53.
[35] Bock J, Töger J, Bidhult S, et al. Validation and reproducibility of cardiovascular 4D-flow MRI from two vendors using 2 × 2 parallel imaging acceleration in pulsatile flow phantom and *in vivo* with and without respiratory gating. Acta Radiol 2019;60:327–37.
[36] Oechtering TH, Nowak A, Sieren MM, et al. Repeatability and reproducibility of various 4D Flow MRI postprocessing software programs in a multi-software and multi-vendor cross-over comparison study. J Cardiovasc Magn Reson 2023;25:22.
[37] Punzo B, Ranieri B, Tramontano L, et al. 4D-Flow cardiovascular magnetic resonance sequence for aortic assessment: multi-vendor and multi-magnetic field reproducibility in healthy volunteers. J Clin Med 2023;12:2960.
[38] Neuhaus E, Weiss K, Bastkowski R, et al. Accelerated aortic 4D flow cardiovascular magnetic resonance using compressed sensing: applicability, validation and clinical integration. J Cardiovasc Magn Reson 2019;21:65.
[39] Dyverfeldt P, Bissell M, Barker AJ, et al. 4D flow cardiovascular magnetic resonance consensus statement. J Cardiovasc Magn Reson 2015;17:72.
[40] Bissell MM, Raimondi F, Ait Ali L, et al. 4D Flow cardiovascular magnetic resonance consensus statement: 2023 update. J Cardiovasc Magn Reson 2023;25:40.
[41] Niemann A, Behme D, Larsen N, et al. Deep learning-based semantic vessel graph extraction for intracranial aneurysm rupture risk management. Int J Comput Assist Radiol Surg 2023. https://doi.org/10.1007/s11548-022-02818-6. Epub ahead of print 10 January.
[42] Chen JV, Dang ABC, Dang A. Comparing cost and print time estimates for six commercially-available 3D printers obtained through slicing software for clinically relevant anatomical models. 3D Print Med 2021;7:1.
[43] Cogswell PM, Rischall MA, Alexander AE, et al. Intracranial vasculature 3D printing: review of techniques and manufacturing processes to inform clinical practice. 3D Print Med 2020;6:18.
[44] Suzuki T, Takao H, Fujimura S, et al. Selection of helical braided flow diverter stents based on hemodynamic performance and mechanical properties. J NeuroInterventional Surg 2017;9:999–1005.
[45] Júnior JR, Telles JPM, Da Silva SA, et al. Epidemiological analysis of 1404 patients with intracranial aneurysm followed in a single Brazilian institution. Surg Neurol Int 2019;10:249.
[46] Maruo S. Stereolithography and two-photon polymerization. In: Sugioka K, editor. Handbook of laser Micro- and Nano-Engineering. Cham: Springer International Publishing; 2021. p. 1–25.
[47] Sindeev S, Arnold PG, Frolov S, et al. Phase-contrast MRI *versus* numerical simulation to quantify hemodynamical changes in cerebral aneurysms after flow diverter treatment. PLOS ONE 2018;13:e0190696.
[48] Berg P, Saalfeld S, Janiga G, et al. Virtual stenting of intracranial aneurysms: a pilot study for the prediction of treatment success based on hemodynamic simulations. Int J Artif Organs 2018;41:698–705.
[49] Baharoglu MI, Schirmer CM, Hoit DA, et al. Aneurysm inflow-angle as a discriminant for rupture in sidewall cerebral aneurysms: morphometric and computational fluid dynamic analysis. Stroke 2010;41:1423–30.
[50] Nariai Y, Takigawa T, Kawamura Y, et al. Inflow angle and height-width ratio are predictors of incomplete occlusion at one and two years after flow diverter treatment for small- and medium-sized internal carotid artery aneurysms. World Neurosurg 2023;180:e716–28.
[51] Fu M, Peng F, Niu H, et al. Inflow angle impacts morphology, hemodynamics, and inflammation of side-wall intracranial aneurysms. J Magn Reson Imaging 2023;57:113–23.
[52] Larsen N, Flüh C, Saalfeld S, et al. Multimodal validation of focal enhancement in intracranial aneurysms as a surrogate marker for aneurysm instability. Neuroradiology 2020;62:1627–35.
[53] Kim T, Lee Y-G. Shape transformable bifurcated stents. Sci Rep 2018;8:13911.
[54] Kim JH, Ha D-H, Han ES, et al. Feasibility and safety of a novel 3D-printed biodegradable biliary stent in an *in vivo* porcine model: a preliminary study. Sci Rep 2022;12:15875.
[55] Elahinia M, Shayesteh Moghaddam N, Taheri Andani M, et al. Fabrication of NiTi through additive manufacturing: a review. Prog Mater Sci 2016;83:630–63.
[56] Demange MK, Von Keudell A, Probst C, et al. Patient-specific implants for lateral unicompartmental knee arthroplasty. Int Orthop 2015;39:1519–26.
[57] Ullah M, Bibi A, Wahab A, et al. Shaping the future of cardiovascular disease by 3D printing applications in stent technology and its clinical outcomes. Curr Probl Cardiol 2024;49:102039.
[58] Wang C, Zhang L, Fang Y, et al. Design, characterization, and 3D printing of cardiovascular stents with zero poisson's ratio in longitudinal deformation. Engineering 2021;7:979–90.
[59] Xiao R, Feng X, Liu W, et al. Direct 3D printing of thin-walled cardiovascular stents with negative Poisson's ratio (NPR) structure and functional metallic coating. Compos Struct 2023;306:116572.